ACS APPLIED MATERIALS & INTERFACES

www.acsami.org

Research Article

Growth Control of Metal–Organic Framework Films on Marine Biological Carbon and Their Potential-Dependent Dopamine Sensing

Xinyi Ke, Zhe Zhao,* Jiayuan Huang, Chang Liu, Gaoshan Huang,* Ji Tan, Hongqin Zhu, Zhijia Xiao, Xuanyong Liu, Yongfeng Mei, and Junhao Chu

Cite This: *ACS Appl. Mater. Interfaces* 2023, 15, 12005–12016

Read Online

ACCESS | Metrics & More | Article Recommendations | Supporting Information

ABSTRACT: Ever-evolving advancements in films have fueled many of the developments in the field of electrochemical sensors. For biosensor application platforms, the fabrication of metal–organic framework (MOF) films on microscopically structured substrates is of tremendous importance. However, fabrication of MOF film-based electrodes always exhibits unsatisfactory performance, and the mechanisms of the fabrication and sensing application of the corresponding composites also need to be explored. Here, we report the fabrication of conformal MIL-53 (Fe) films on carbonized natural seaweed with the assistance of an oxide nanomembrane and a potential-dependent electrochemical dopamine (DA) sensor. The geometry and structure of the composite can be conveniently tuned by the experimental parameters, while the sensing performance is significantly influenced by the applied potential. The obtained sensor demonstrates ultrahigh sensitivity, a wide linear range, a low limit of detection, and a good distinction between DA and ascorbic acid at an optimized potential of 0.3 V. The underneath mechanism is investigated in detail with the help of theoretical calculations. This work bridges the natural material and MOF films and is promising for future biosensing applications.

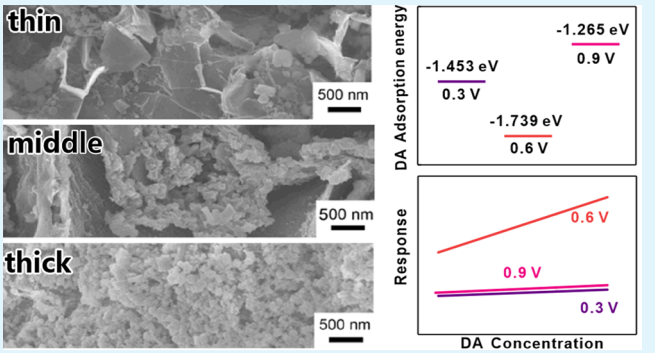

KEYWORDS: *metal–organic frameworks, assembled film, biosensor, dopamine, carbon-based composite*

INTRODUCTION

With the advent of the post-Moore age in recent years, biosensing research has increasingly intensified.[1−4] Among all kinds of biosensors, effective detection of dopamine (DA) (a catecholamine in the central nervous system related to Alzheimer's and Parkinson's) is crucial for human health.[5] Various detection approaches have been developed, including high-performance liquid chromatography,[6] mass spectrometry,[7] spectrophotometry,[8] Fourier transform infrared spectroscopy,[9] and electrochemical methods.[10,11] Among the reliable approaches, electrochemical methods are the most sensitive and the simplest.[12] So far, one of the major issues with electrochemical measurements of DA stems from interference from other biological compounds, most typically ascorbic acid (AA), which always coexists in biological samples containing DA. Most conventional electrodes show a lack of selectivity due to the overlap of the DA signal with AA.[13] Therefore, optimizing the sensor performance (e.g., high sensitivity and remarkable selectivity) via tuning structural and experimental parameters and exploring the corresponding sensing mechanism are particularly important in electrochemical DA sensing.

In the field of electrochemical sensing, materials with hierarchical structures and large surface areas that are highly conductive are likely to have superior performance.[14−17] Nevertheless, artificial multilayered and porous materials that meet these standards are typically costlier and more difficult to be fabricated. Therefore, researchers attempted to construct low-cost and high-volume substrates by combining carbonized natural materials with functional materials such as metal–organic frameworks (MOFs).[18,19] MOFs are well known for their typical characteristics, including large specific surface areas, ultrahigh porosities, and excellent thermal and chemical stabilities.[20,21] Previously, Kim et al.[22] detailed protocols for synthesizing high-quality ZIF-8 and its modified forms of hollow ZIF-8, core–shell ZIF-8@ZIF-67, and ZIF-8@mesostructured polydopamine, which could be widely utilized in

Received: November 15, 2022
Accepted: February 12, 2023
Published: February 24, 2023

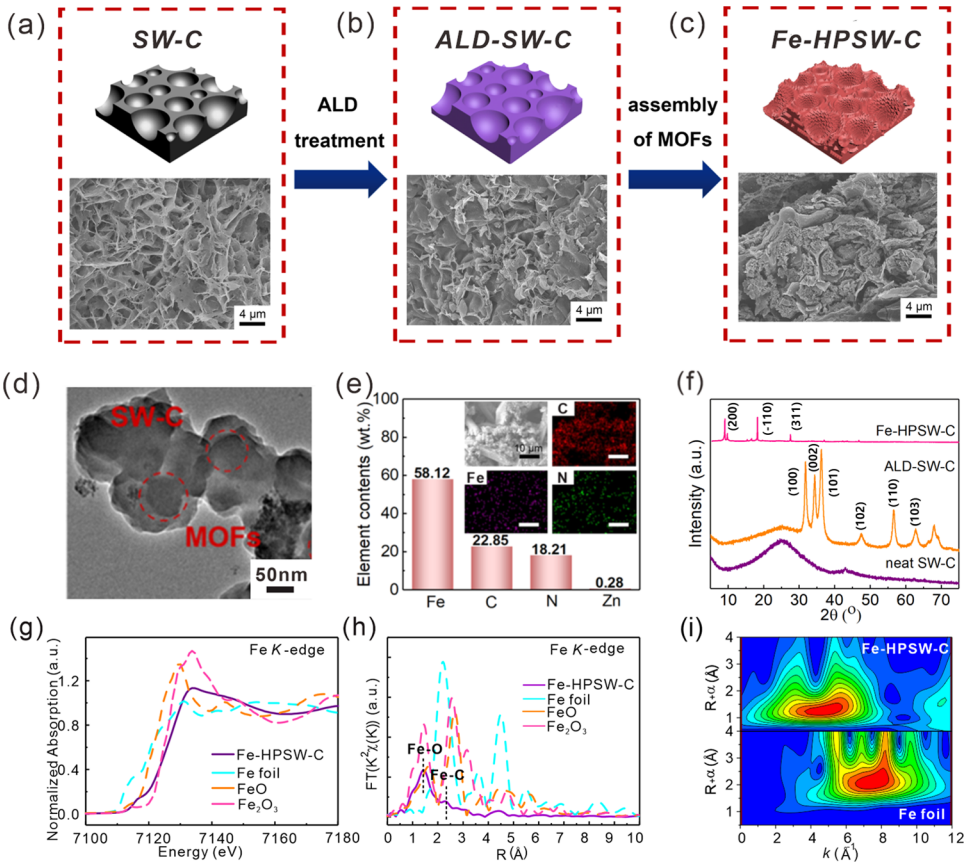

Figure 1. (a–c) Schematic of the fabrication process and SEM images of SW-C, ALD-SW-C, and Fe-HPSW-C. (d) TEM image of Fe-HPSW-C. (e) Elemental content of Fe-HPSW-C. The inset shows the EDS mapping images of Fe-HPSW-C. Scale bar: 10 μm. (f) XRD patterns of neat SW-C, ALD-SW-C, and Fe-HPSW-C. (g) Fe K-edge XANES spectra of HPSW-C and its references. (h) FT k^3-weighted EXAFS spectra of Fe-HPSW-C and its references. (i) WT analysis of Fe-HPSW-C and Fe foil.

electrochemical applications. Shahrokhian and co-workers fabricated a sensitive and fast response electrochemical glucose sensing platform based on Co-based MOFs obtained from rapid in situ conversion of electrodeposited cobalt hydroxide intermediates.[23,24] This team also prepared an electrochemical device based on MOFs for electrocatalytic oxidation of L-cysteine, which could benefit the fabrication of a high-performance nonenzymatic biosensing platform.[25] Huo et al.[26] developed a modulator-induced strategy for fabricating transitional MOFs with carboxylic ligands by building an esterification reaction, and the modified Pt/solid-transitional MOF catalyst exhibited outstanding performance in the cycloaddition reaction. Nevertheless, preparation of uniform MOF films on a substrate with complex geometry is still difficult for the community. In our previous work, we employed an effective strategy to prepare MOF films with the assistance of oxide nanomembranes prepared by atomic layer deposition (ALD).[27] Taking the advantages of the high uniformity, high controllability, and good conformality of ALD, we can fabricate MOF films on three-dimensional (3D) substrates with firm adhesion. The fabricated MOF film with outstanding electrochemical performance may be utilized for effective DA sensing, as demonstrated by our earlier research.[27] However, for a natural material substrate, the approach is still facing challenges due to enormous defects and imperfections of the substrate, and thus, effort to understand the growth mechanism is required to realize controllable growth on a broad range of substrates. In addition, from the viewpoint of sensing application, further research is needed to disclose the electrochemical properties. Performance optimization from the aspect of a molecular redox process to achieve high sensitivity between DA and AA also requires more research input.

Herein, we use marine biological carbon (carbonized seaweed) as the substrate to prepare Fe-doped MOFs (i.e., MIL-53 (Fe)) to form the so-called Fe-doped hierarchically porous seaweed carbon (Fe-HPSW-C) sensing electrode with the assistance of an ALD ZnO nanomembrane. As a natural material, seaweed-derived carbon has a random framework structure with inherent porosity, which not only provides electron transfer highway but also confines the target biomolecules by its inner pores.[28] On the other hand, MIL-53 (Fe) can provide high active site exposure and many catalytically active ions for enhancing sensitivity. During the experiment, growth control of MOF films is achieved by adjusting the solvent concentration and parameters of the ALD process, and a uniform MOF film is obtained on the complex substrate. We explore the electrochemical properties of differently structured MOF films in detail and achieve high sensitivity toward DA at an optimized potential. Quantitatively, Fe-HPSW-C exhibits a good sensitivity of 2084.58 μA mM^{-1} cm^{-2} with a low limit of detection (LOD) of 0.73 μM toward DA. Also, effective discrimination of DA and AA is also achieved. The great sensing performance may be ascribed to the unique composite structure with optimized geometry. In addition, theoretical calculations are utilized to explain the experimental phenomenon and reaction mechanism. Through

https://doi.org/10.1021/acsami.2c20517
ACS Appl. Mater. Interfaces 2023, 15, 12005−12016

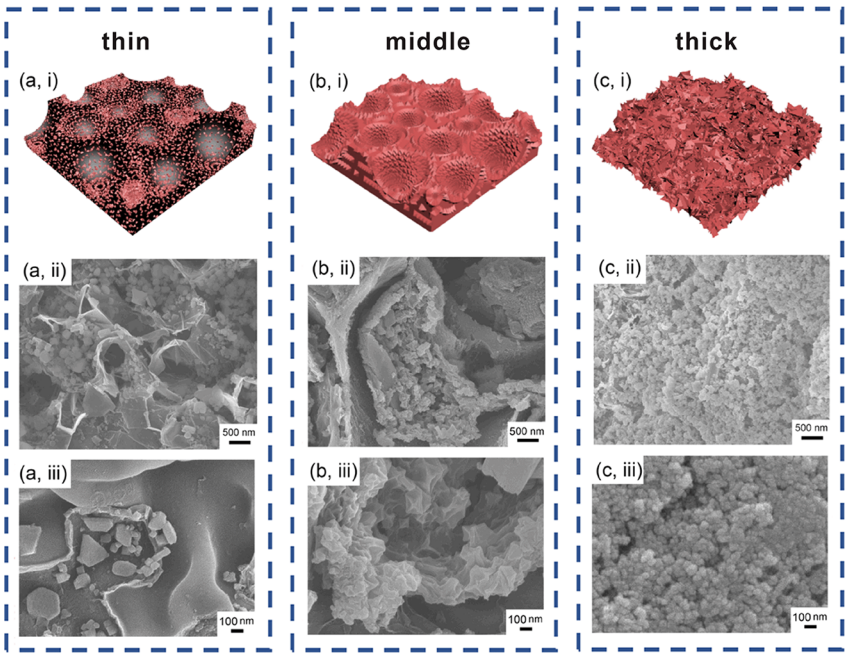

Figure 2. Schematic illustrations of Fe-HPSW-C composites with different MIL-53 (Fe) film thicknesses. Panels (a–c) represent a thin film, a middle-thickness film, and a thick film, respectively. Panels (i–iii) are the corresponding schematics, SEM images at low magnification, and SEM images at large magnification, respectively.

the in-depth study of the biosensing mechanism, this work also gives a novel notion for the preparation of nonenzymatic sensing electrodes in biosensing-related fields, thereby widening the application in chip-based devices.[29]

RESULTS AND DISCUSSION

Figure 1a–c shows the schematic demonstration and scanning electron microscopy (SEM) images of the synthesis process of Fe-HPSW-C. During the carbonization process in a N_2 atmosphere (Figure 1a, SW-C (seaweed-carbonized)), the organic components of the seaweed transform into conductive carbon with volume shrinkage while preserving the bio-morphology and flexibility. Then, on the surface of this complex structure, a ZnO nanomembrane is deposited by ALD to assist subsequent preparation of MOF film with firm adhesion (Figure 1b, ALD-SW-C). The adhesion force between the ZnO nanomembrane and the substrate endows outstanding structural stability, which optimizes the whole fabrication process. After the growth of the ZnO nano-membrane by ALD (Figure S1, with a typical nanomembrane thickness of 50 nm), MIL-53 (Fe) films are conformally grown on the surface of ALD-SW-C by a liquid-phase fabrication process, where MOF particles are assembled into a dense film (Figure 1c). According to our previous reports, the whole chemical reaction may possibly be concluded by the following two equations[27]

$$ZnO + 2FeCl_3{\cdot}6H_2O \rightarrow [(Zn,\ Fe_2)(OH)_2]Cl_6{\cdot}11H_2O \quad (1)$$

$$[(Zn,\ Fe_2)(OH)_2]Cl_6{\cdot}11H_2O + H_2BDC \rightarrow 2MIL-53\ (Fe) + Zn^{2+} + 6Cl^- + 4H^+ \quad (2)$$

Here, the ALD process forms a multicrystal ZnO nano-membrane (see below), which provides vast nucleation sites for the following assembly of the MOF film. The as-prepared MIL-53 (Fe) film tightly wraps around the 3D structure of SW-C, forming a uniform layer. The film remains after 1 h of ultrasonication treatment, proving firm adhesion therein. We also grow MIL-53 (Fe) films on Si substrate with the assistance of ALD ZnO nanomembranes. As displayed in Figure S2, the intrinsic morphology of MIL-53 (Fe) particles can be observed. In this work, the morphology and structure of Fe-HPSW-C are further investigated by transmission electron microscopy (TEM), which confirms the polyhedral morphology and good dispersion (Figures 1d and S3), and intimate contact between the SW-C substrate and MIL-53 (Fe) can be observed. Figure 1e shows the energy-dispersive spectroscopy (EDS) results of the composite, clearly demonstrating C, Fe, N, and Zn with high concentrations in the composite. The insets of Figure 1e show the energy-dispersive spectroscopy (EDS) mapping images of the elements. One can see that the elements are evenly distributed on the surface of the composite, implying the uniform growth of the MIL-53 (Fe) film. To further study the structure of the samples, X-ray diffraction (XRD) patterns of neat SW-C, ALD-SW-C, and Fe-HPSW-C were obtained and are shown in Figure 1f. The broad peak at 20–30° belongs to the C substrate, while peaks of Fe-HPSW-C at 10–70° match well with the MIL-53 (Fe) structure. Especially, three sharp peaks associated with the (200), (−110), and (311) lattice planes of MIL-53 (Fe) can be observed from XRD patterns of Fe-HPSW-C,[30,31] further confirming the successful growth of the MIL-53 (Fe) film on the 3D substrate. In addition, it is worth noting that the diffraction of ALD-SW-C is different from that of neat SW-C, indicating the formation of a new phase. Here, the existence of a multicrystal ZnO nanomembrane by ALD can be proved by diffraction peaks at 2θ = 31.7, 34.32, 36.22, 47.58, 56.58, and 62.76°, which are respectively associated with the (100), (002), (101), (102), (110), and (103) lattice planes of hexagonal ZnO.[32]

https://doi.org/10.1021/acsami.2c20517
ACS Appl. Mater. Interfaces 2023, 15, 12005–12016

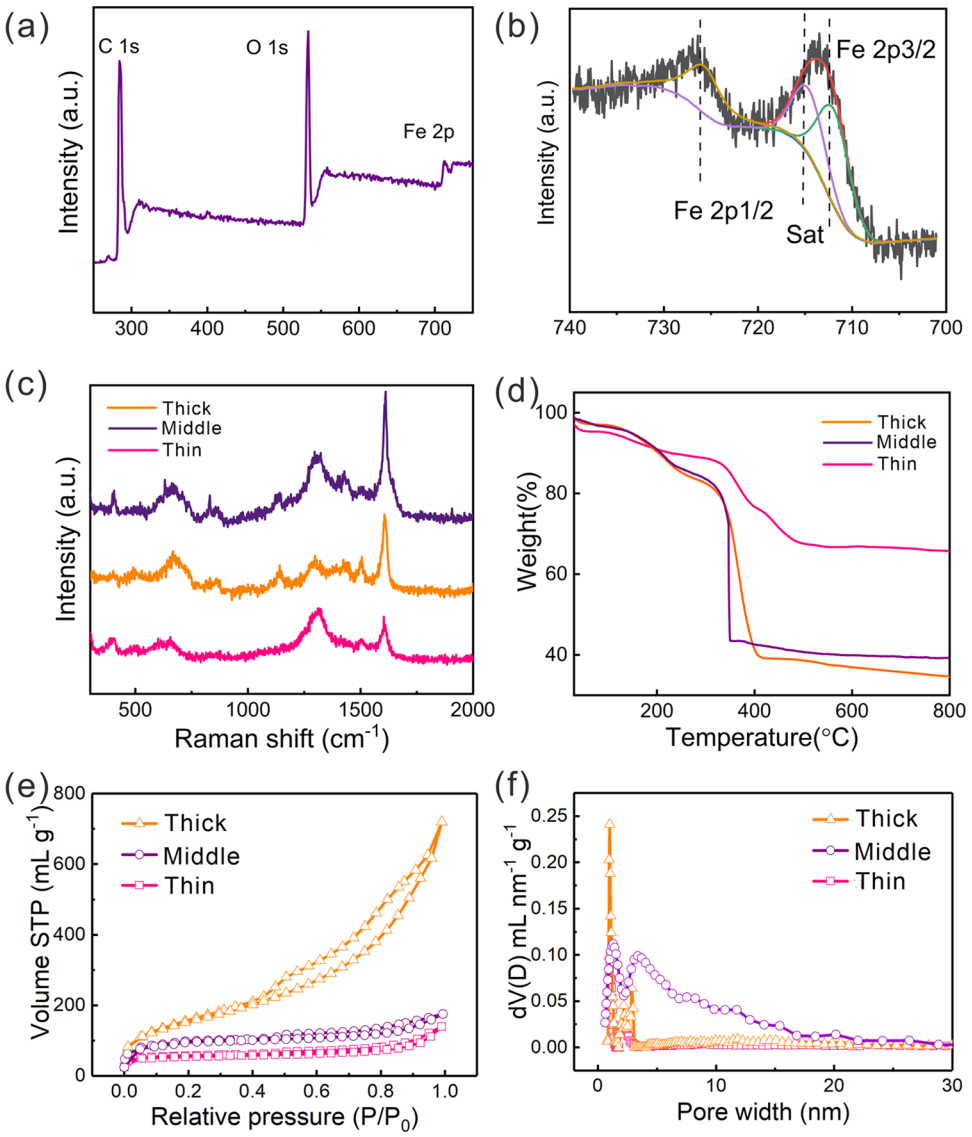

Figure 3. (a) XPS survey scan of the Fe-HPSW-C composite. (b) Corresponding high-resolution Fe 2p XPS spectrum. (c) Raman spectra of Fe-HPSW-C composites with different MIL-53 (Fe) film thicknesses. (d) TGA curves of Fe-HPSW-C composites with different MIL-53 (Fe) film thicknesses. (e) Nitrogen adsorption/desorption isotherms for Fe-HPSW-C composites with different MIL-53 (Fe) film thicknesses. (f) Calculated pore size distributions of Fe-HPSW-C composites with different MIL-53 (Fe) film thicknesses.

To gain more insights into the electronic structure and coordination environment of the Fe atoms in Fe-HPSW-C, X-ray absorption near-edge structure (XANES) and extended X-ray absorption fine structure (EXAFS) spectra were collected (Figure 1g–i). From the Fe K-edge XANES normalization diagram (Figure 1g), it can be seen that the absorption edge of Fe-HPSW-C is located between FeO and Fe_2O_3, indicating that the valence of Fe is between Fe^{2+} and Fe^{3+}, close to Fe^{3+}, and thus, Fe ions can change valence with redox activity. EXAFS spectra of Fe-HPSW-C, FeO, Fe_2O_3, and Fe foil samples in the *k*-space are illustrated to assist analysis in Figure S4. The Fourier transform (FT) k^3-weighted EXAFS spectra (Figure 1h) of Fe-HPSW-C shows a peak at 1.43 Å, corresponding to the scattering contribution of Fe−O, and a peak at 2.32 Å, corresponding to the scattering contribution of Fe−C. Then, the wavelet transform (WT) analysis for the k^3-weighted Fe K-edge EXAFS signal in view of the strong resolution (Figure 1i) is provided both in the radial distance and *k*-space to clearly separate the backscattering atoms. The signal of WT related to Fe−Fe bonds has been detected in the Fe foil (7.8 Å) but not in Fe-HPSW-C, and Fe−N bonds have been detected in Fe-HPSW-C (4.6 Å), strongly indicating that there is only atomically dispersed Fe−O/C in HPSW-C. In addition, the extended edge of EXAFS is further fitted (Figures S5 and S6), and the paths of Fe−O and Fe−C are introduced to confirm the concrete structure (Table S1). The Fe K-edge EXAFS data reveal a Fe−O bond length of 1.87 ± 0.02 Å and a Fe−C bond length of 2.858 Å for HPSW-C, which show great consistency with the literature values.[33] These results demonstrate the numerous coordination types in MIL-53 (Fe) and the correspondingly large number of active sites. The redox reaction of Fe ions can be observed in the following electrochemical tests, where the changed valence is probed by the response current.

Currently, Fe-HPSW-C is prepared by combining hierarchically porous material (SW-C) and the ALD ZnO nanomembrane-induced MIL-53 (Fe) film. Then, we further study the growth of MIL-53 (Fe) in the Fe-HPSW-C composite, as

https://doi.org/10.1021/acsami.2c20517
ACS Appl. Mater. Interfaces 2023, 15, 12005−12016

demonstrated in Figure 2. Figure 2a-i shows the schematic of Fe-HPSW-C with the smallest MIL-53 (Fe) film thickness, while Figure 2a-ii,iii shows the corresponding SEM images at low and high magnifications, respectively. Due to the growth of low-dose MIL-53 (Fe) particles on the substrate as a result of the low-concentration solution in the liquid-phase fabrication process, the morphology depicted in Figure 2a is nonuniform and dispersed. The particles are incapable of effectively wrapping the substrate and forming a film thereon. By increasing the concentration of the solution to an optimal value, the most suitable status is identified by observation. This is proved in Figure 2b, where MIL-53 (Fe) particles are grown uniformly across the substrate, forming a uniform film. Especially at large magnification (Figure 2b-ii), the grown film demonstrates high conformality. We further slice the obtained Fe-HPSW-C with the MIL-53 (Fe) film of a middle thickness (70 nm) and monitor its cross section. From Figure S7, it can be observed more clearly that the film evenly wraps the inner and outer walls of the SW-C. However, when the reactant concentration is too high (i.e., twice the optimal value), MIL-53 (Fe) particles accumulate, forming a thick coating that covers the inherent structure of the 3D substrate (Figure 2c). To achieve more specific growth control, the influence of ZnO nanomembrane thickness (i.e., ALD cycles) is also investigated to disclose more details about the present growth strategy. Figure S8 depicts the SEM images of Fe-HPSW-C obtained with the assistance of different ALD ZnO nanomembranes. To further illustrate the necessity of ALD, substrate SW-C without the ALD ZnO nanomembrane is also employed here for comparison. When MIL-53 (Fe) develops on SW-C treated without the ALD ZnO nanomembrane (i.e., 0 ALD cycle), it is nearly impossible to find MIL-53 (Fe) particles (Figure S8a,b). Also, for SW-C processed with 100 ALD cycles (Figure S8c,d) and 200 ALD cycles (Figure S8e,f), we find incomplete coverage by MIL-53 (Fe) particles. However, after the growth of ZnO with 300 ALD cycles (~50 nm ZnO nanomembrane), conformal growth of the MIL-53 (Fe) layer on the surface of SW-C is seen (Figure S8g,h).

Furthermore, the elements' chemical states in the composite are investigated by X-ray photoelectron spectroscopy (XPS), which confirms the presence of Fe, O, and C (Figure 3a,b).[34] The high-resolution Fe 2p spectrum can be deconvoluted into three peaks at 725.3, 711.4, and 715.7 eV, corresponding to Fe $2p_{1/2}$, Fe $2p_{3/2}$, and satellite species of Fe(III), respectively,[27] and the presence of Fe(III) is considered to be able to provide high oxidation activity for high-performance electrochemical applications.[35] Moreover, four XPS peaks exist in the high-resolution N 1s XPS spectrum (Figure S9), corresponding to pyridinic-N (398.6 eV), pyrrolic-N (399.7 eV), quaternary nitrogen (400.8 eV), and pyridine N-oxide (403 eV), which should originate from the MIL-53 (Fe) film and the substrate.[36] To further characterize the fabricated composites, Raman spectra of the samples with different MIL-53 (Fe) film thicknesses were obtained over a wide range of 300−2000 cm^{-1}, and the results are shown in Figure 3c. A strong Raman peak associated with ν (C═C), a typical aromatic cyclic bond, appears at 1619 cm^{-1}. Also, Raman peaks at around 447, 639, 860, 1151, and 1504 cm^{-1} are ascribed to the characteristic vibrations of MIL-53 (Fe).[37] Except for the weak signal from the thin MIL-53 (Fe) film, none of the three spectra changed substantially, indicating that the thickness does not have much effect on the structure of the MIL-53 (Fe) film. The thermal gravimetric analysis (TGA) of Fe-HPSW-C composites was performed to estimate the thermal stability of the composites, and the samples were heated to 800 °C in a N_2 atmosphere. As illustrated in Figure 3d, at temperatures above 300 °C, a decrease in mass, possibly caused by the loss of OH/O/F terminated groups,[38] can be seen, which proves the outstanding structural stability of Fe-HPSW-C for applications in a wide temperature range. In addition, the TGA results also indicate a high Fe content in the composite, and this is beneficial for electrochemical sensing.[27,39] To investigate the pore structure of the composites, nitrogen adsorption−desorption isotherms and corresponding pore size distributions of samples with different MIL-53 (Fe) film thicknesses are shown in Figure 3e,f. All of the fabricated samples demonstrate both type I isotherms, corresponding to the microporous structure, and type IV isotherms, corresponding to the mesoporous structure. The results thus indicate a hierarchically porous structure composed of micropores and mesopores in the composite. The micropores are inherited from the pores in the MOF structure, and the stacking of MOF particles results in the formation of mesopores in the MOF film.[40] In addition, the specific pore size distribution is calculated on the basis of the Barrett−Joyner−Halenda (BJH) method, and the micro/mesopore ratio is analyzed by nonlocal density functional theory (NLDFT).[41,42] The obtained results are demonstrated in Figure 3f. Consistent with isotherms, open mesopores with an average size of ~4 nm exist in Fe-HPSW-C with different MIL-53 (Fe) film thicknesses, which could facilitate electrolyte penetration.[43] Also, micropores with an average size of ~2 nm can be clearly observed in the middle-thickness MIL-53 (Fe) film, which helps to expose the active sites.[43] The detailed pore structures of Fe-HPSW-C with different thicknesses are summarized in Table 1. The composite with a thin MIL-53 (Fe) film provides a specific surface area of 193 $m^2\ g^{-1}$, as determined by Brunauer−Emmett−Teller (BET). The composite with a middle-thickness MIL-53 (Fe) film illustrates an increased specific surface area of 313 $m^2\ g^{-1}$, and the composite with a thick MIL-53 (Fe) film exhibits the largest BET surface area of 552 $m^2\ g^{-1}$. It is worth mentioning that the surface area of the MIL-53 (Fe) film is smaller than that of MIL-53 (Fe) particles,[44] and the difference is ascribed to the different pore structures and stacking of MOF nanoparticles, as mentioned above. We should stress that the hierarchically porous structure with the large surface area of the Fe-HPSW-C composite might play essential roles in enhancing the sensing performance,[45] as will be demonstrated later.

Table 1. Specific Surface Area and Pore Size Distribution of Fe-HPSW-C with Different MIL-53 (Fe) Film Thicknesses

sample	surface area ($m^2\ g^{-1}$)	total pore volume (mL g^{-1})	micropore volume (mL g^{-1})	mesopore volume (mL g^{-1})
thin	193	0.17	0.061	0.109
middle	313	0.24	0.093	0.147
thick	552	0.93	0.12	0.81

Although the sample with the largest thickness possesses the largest pore volume and surface area, its electrochemical property may be worse than that of the sample with the middle-thickness MIL-53 (Fe) film. It is worth noting that thick MIL-53 (Fe) film exhibits a volume ratio ($V_{mesopores}/V_{total\ pores}$) of nearly 0.1, and such a large number of mesopores will decline the electron transfer, leading to deteriorated

https://doi.org/10.1021/acsami.2c20517
ACS Appl. Mater. Interfaces 2023, 15, 12005−12016

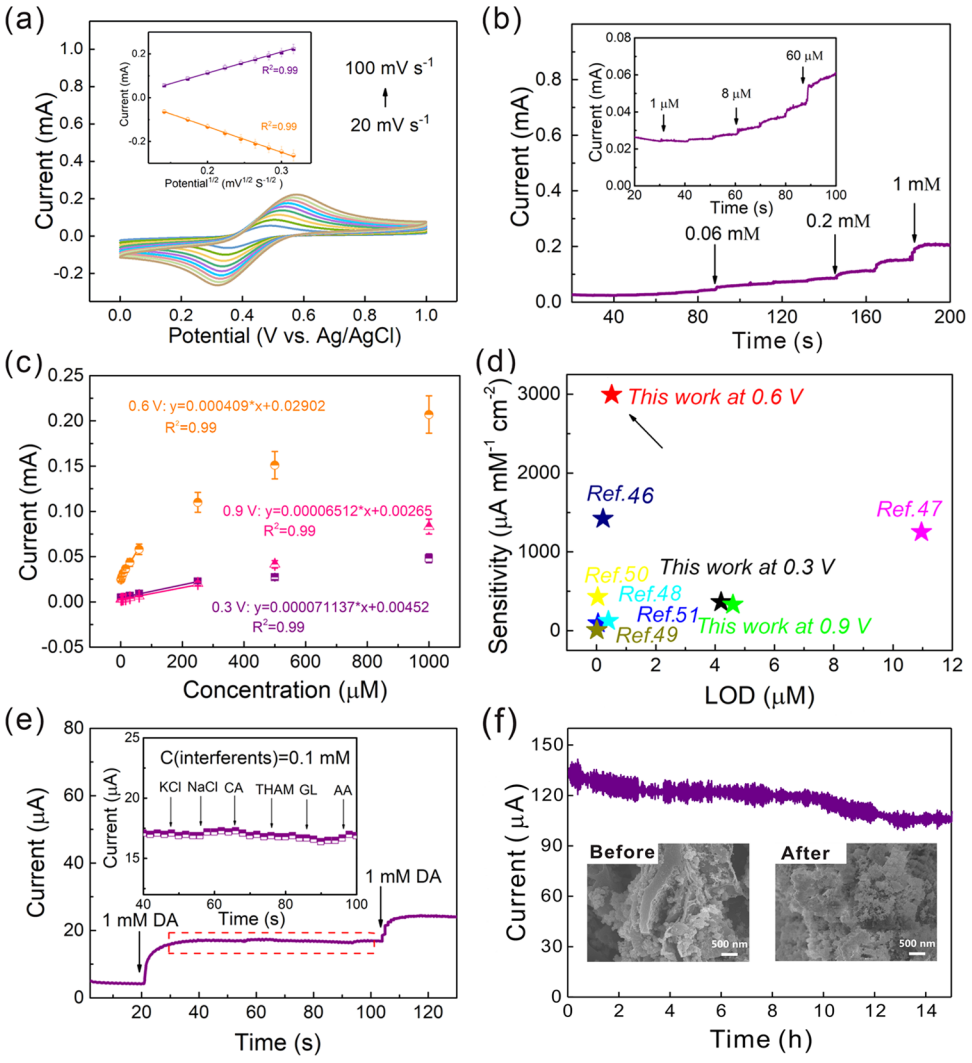

Figure 4. Electrochemical performance of the Fe-HPSW-C composite with the middle-thickness MIL-53 (Fe) film. (a) CV scans at various scan rates of 20−100 mV s^{-1} in 0.1 M PBS (pH = 7.2) containing 5 mM $K_3[Fe(CN)_6]$. The inset shows the oxidation peak current (purple line) and reduction peak current (orange line) of Fe-HPSW-C as a function of the square root of the scan rate, derived from CV scans. (b) *I*−*t* curve of the Fe-HPSW-C composite with the successive addition of DA in 0.1 M PBS at a potential of 0.6 V. The inset shows an enlarged image. (c) Calibration plot where the testing potentials are 0.3, 0.6, and 0.9 V. (d) Summary of DA sensing performance of the MOF-based structure reported in the literature published in recent years.[46−51] (e) *I*−*t* curve of Fe-HPSW-C for the continuous addition of 1 mM DA, 0.1 mM KCl, 0.1 mM NaCl, 0.1 mM CA, 0.1 mM THAM, 0.1 mM LA, 0.1 mM GL, 0.1 mM AA, and 1 mM DA at 0.6 V. (f) *I*−*t* curve of Fe-HPSW-C in 0.1 M PBS with 1.0 mM DA at 0.6 V for the 15 h stability test. The inset shows the SEM images of Fe-HPSW-C before and after the stability test.

performance. Thus, the Fe-HPSW-C composite with the middle-thickness MIL-53 (Fe) film was investigated in most of the following investigations. To quantitatively study the electrochemical activity, the active area of the composite was first investigated using $K_3[Fe(CN)_6]$ as a probe. As shown in the inset of Figure 4a, oxidation and reduction peaks can be observed in the cyclic voltammetry (CV) scans of the electrode (i.e., the Fe-HPSW-C composite with the middle-thickness MIL-53 (Fe) film), and the oxidation and reduction peak currents increase as the scan rate increases from 20 to 100 mV s^{-1}. Then, the active area (*S*) of the electrode material can be calculated by the Randles−Sevcik equation

$$I_{peak} = (2.69 \times 10^5) n^{3/2} S D^{1/2} C v^{1/2}$$

where *n* is the number of transferred electrons, *D* is the diffusion coefficient of $K_3[Fe(CN)_6]$, and *C* is the bulk concentration of $K_3[Fe(CN)_6]$.[46] Herein, the value of *S* is evaluated as 0.0288 cm^2 based on the slope of the peak current versus the square root of the scan rate (Figure 4a). This result demonstrates the high surface area and high active site exposure of the Fe-HPSW-C composite.

Cyclic voltammetry (CV) scans of the electrode (middle-thickness MIL-53 (Fe) film) in 0.1 M PBS (pH = 7.2) containing DA of different concentrations are also used for evaluation. As shown in Figure S10, oxidation and reduction peaks, located at 0.0484 and 0.0512 mA, respectively, can be observed, and the oxidation and reduction peak currents increase as the concentration of DA increases from 0 to 8 mM. The underneath mechanism of DA sensing is presumably based on the following equation

$$\text{MIL} - 53(\text{Fe(III)}) - 2e^- + C_8H_9N(OH)_2 \rightleftharpoons \text{MIL} - 53(\text{Fe(II)}) + C_8H_9NO_2 + 2H^+ \quad (3)$$

https://doi.org/10.1021/acsami.2c20517
ACS Appl. Mater. Interfaces 2023, 15, 12005−12016

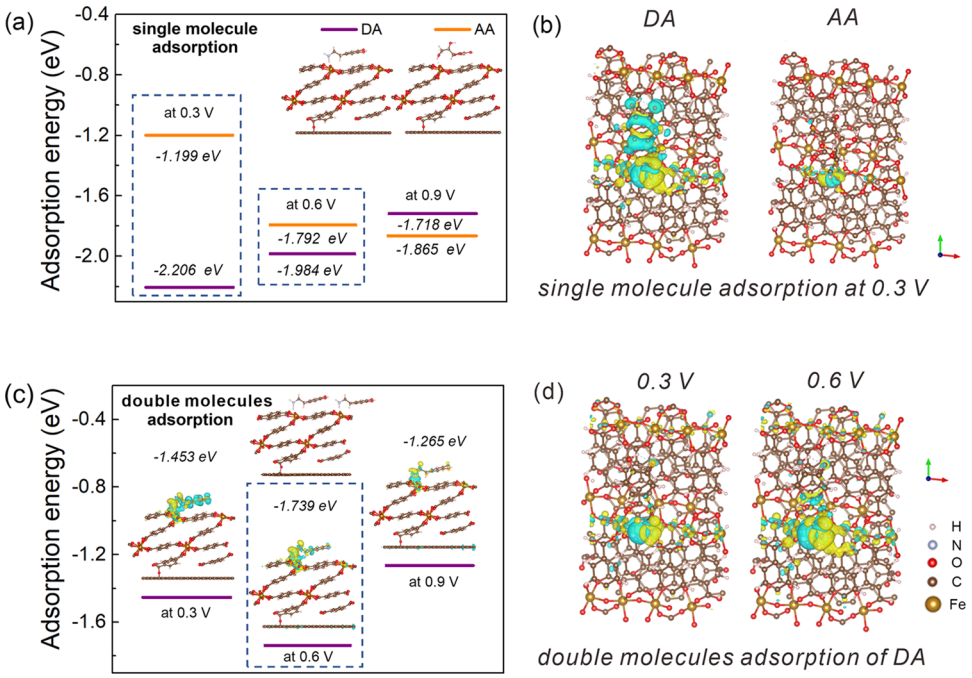

Figure 5. Schematic diagrams of DA and AA adsorption mechanisms under different potentials. (a) Single-molecule adsorption energies of DA and AA at 0.3, 0.6, and 0.9 V. The inset shows the optimized structures of DA and AA adsorbed on MIL-53 (Fe). (b) Top views of the difference in charge densities for the single adsorption configuration of DA and AA at 0.3 V, in which blue and yellow regions indicate electron depletion and accumulation, respectively. (c) Double-molecule adsorption energies of DA at 0.3, 0.6, and 0.9 V. The inset shows the optimized structure of double DA molecules adsorbed by MIL-53 (Fe). Side views of the difference in charge densities for double-molecule adsorption of DA at 0.3, 0.6, and 0.9 V are also shown in the insets. (d) Top view of the difference in charge densities for the second adsorption configuration of DA at 0.3 and 0.6 V, in which blue and yellow regions indicate electron depletion and accumulation, respectively.

In addition, we use current−time (I−t) measurements to evaluate the electrochemical sensing performance and identify the appropriate potential for DA sensing. Figure 4b and its inset illustrate the I−t curve of the electrode (middle-thickness MIL-53 (Fe) film) by successively adding different concentrations of DA in 0.1 M PBS. A distinct and rapid current response can be observed with the addition of DA, indicating good real-time sensing capability. On the other hand, Figure S11 shows the corresponding I−t curve of composites with the thick and thin MIL-53 (Fe) films, and both samples show worse response, which is ascribed to a large number of mesopores and the low surface area, respectively.[40] We also compared the sensing performance of the composite prepared with and without ALD ZnO nanomembrane. As shown in Figure S12, the Fe-HPSW-C composite exhibits an apparent response toward DA, while the composite without the ZnO nanomembrane shows negligible sensing performance. This indicates that without the ALD ZnO nanomembrane, the low loading of MIL-53 (Fe) on the substrate should result in a small number of active sites in the composite, causing poor sensitivity of the sensor. Moreover, the sensing performance of the sample under different potentials is also studied (I−t curves under 0.3 and 0.9 V shown in Figure S13a,b). Analyses of the three sets of data lead to the corresponding calibration plots as a function of concentration, as shown in Figure 4c. According to the calibration plot, the composite exhibits an ultrahigh sensitivity of 2084.58 μA mM^{-1} cm^{-2} with a linear range of 1.0−200 μM (linear regression equation: Y = 0.000409X + 0.02902; correlation coefficient (R^2) = 0.99). The LOD can be calculated by the following equation: LOD = 3δ/S, where δ is the standard deviation and S is the sensitivity, and thus, a low LOD of 0.73 μM is obtained. We stress that these values can compare favorably with those of numerous other MOF-based electrochemical DA sensors described in previous papers.[46−51] A detailed comparison of the sensing performance is summarized in Figure 4d, and a more comprehensive comparison can be found in Table S2, indicating the advances of this strategy. It is considered that the observed ultrahigh sensitivity can be associated with the following factors:[52−54] (i) assembly of MIL-53 (Fe) particles on the 3D substrate enhances the utilization of the structural advantages, (ii) hierarchically porous structure increases the exposure of electrochemically active sites, (iii) 3D conductive carbon substrate provides a highway for charge transfer, which reduces the low conductivity drawback of MOFs, and (iv) hierarchically porous structure enhances the capture of target biomolecules. Without these factors, the materials cannot exhibit outstanding electrochemical performance. Experimentally, we compare electrochemical responses of neat SW-C, ALD-SW-C, pure MIL-53 particles, and Fe-HPSW-C (middle-thickness MIL-53 (Fe) film) toward DA (Figure S14). Obviously, Fe-HPSW-C shows much better electrochemical properties compared to MIL-53 particles, while neat SW-C and ALD-SW-C, which lack the redox element (i.e., MIL-53 (Fe)), exhibit undetectable response.

Anti-interference ability is also important for evaluating sensing performance.[55] Figure 4e shows the I−t curve with continuous addition of 1.5 mM DA, 0.1 mM KCl, 0.1 mM NaCl, 0.1 mM citric acid (CA), 0.1 mM tromethamine (THAM), 0.1 mM glucose (GL), and 0.1 mM AA. One can see that the interferents generate only a tiny current response related to DA, demonstrating a strong anti-interference capability. The stability of the electrochemical sensor based on the Fe-HPSW-C composite is further evaluated in a PBS

https://doi.org/10.1021/acsami.2c20517
ACS Appl. Mater. Interfaces 2023, 15, 12005−12016

solution containing 1 mM DA at 0.6 V. As shown in Figure 4f, the composite exhibits a current response of ~0.12 mA with good stability within 15 h. SEM images (inset of Figure 4f) and XRD patterns (Figure S15) of the Fe-HPSW-C composite before and after the stability test further prove the structural stability of Fe-HPSW-C. In addition, the selectivity of Fe-HPSW-C is illustrated in Figure S16, and at 0.3 and 0.6 V, the $I-t$ curves of the composite with successive additions of 1 mM DA and 3 mM interferents (e.g., NaCl, KCl, LA, GL, and THAM) reveal a considerable current response upon addition of target DA. It is noticed that, in biological tissues, the presence of significant quantities of AA influences the electrochemical detection of DA, resulting in a considerable overpotential for oxidation by conventional electrodes.[55] Therefore, the distinction between DA and AA is essential for electrochemical DA sensors. In this work, we test AA and DA with the same concentration under different potentials (0.3, 0.6, and 0.9 V). As shown in Figure S17a, at 0.3 V, with the successive addition of 1 mM DA and 1 mM AA, the response of the composite to DA was more than three times larger than that to AA, indicating the selective determination of DA. However, when tested at 0.6 or 0.9 V, the response of the composite electrode to DA was nearly identical to that to AA (Figure S17b,c). Moreover, the repeatability of the sensor is determined by measuring 1 mM DA six times with the same sensor. As demonstrated in Figure S18, the overlap of the $I-t$ curves indicates an identical response, and the relative standard deviation (RSD) is 2.6% (inset of Figure S18), demonstrating excellent repeatability. The CV responses of the same Fe-HPSW-C composite toward DA are also measured six times (Figure S19), and the RSD is calculated to be 1.98% (Figure S20), again demonstrating the good accuracy of the sensor. We also employed biological samples (urine and juice) to validate the sensing performance in practice. Figure S21a depicts the $I-t$ curve of Fe-HPSW-C with serial additions of urine in 0.1 M PBS, where the response to urine can be clearly observed. In contrast, nearly no current change is detected with multiple additions of juice with the same volume (Figure S21b). With serial additions of urine and juice, it is only possible to detect a significant rise in current in the case of urine (Figure S21c). All of the results are consistent with the laboratory, illustrating the good sensitivity and selectivity of Fe-HPSW-C in practical applications.

We notice that the current response of the composite is different at various potentials, which may be related to the molecule activity on the catalyst surface, and the adsorption energy is considered to be a major influencing factor.[40,53] Here, calculations based on density functional theory (DFT) are performed to gain further insight into the high activity and selectivity of DA under specific potentials. Figure 5a,b demonstrates the adsorption configuration of single-molecule DA and AA. Both the top view and side view of the difference in charge densities for the single-molecule adsorption configuration of the minimal repeating unit of DA and AA illustrate the larger strength effect of DA (Figures 5b, S22, and S23). For single DA adsorption, the required adsorption energy decreases as the potential increases. The adsorption energies of DA under 0.3, 0.6, and 0.9 V are −2.206, −1.984, and −1.717 eV, respectively (Figure 5a). However, for AA adsorbed under the same situation, the adsorption configuration of AA molecules changes remarkably and the adsorption energy increases as the potential increases, which can be observed in Figure 5a. This phenomenon can be explained by the structure difference between the two molecules. The DA molecule possesses fewer oxygen atoms on the right side of the ring (i.e., lower electronegativity), and the ring configuration generates a π bond that can delocalize and share the charge, making the DA molecule less potential-sensitive. Compared with DA, the ring of AA with fewer oxygen atoms on it means greater electronegativity. Thus, the influence of potential is more pronounced for the AA molecule (Figure S23). We consider that the observed good selectivity at 0.3 V could be due to the difference in absorption energy because the number of molecules adsorbed on the electrode surface are different correspondingly. Specifically, at 0.3 V, the single-molecule adsorption energies of AA and DA are −2.206 and −1.199 eV, respectively (Figure 5a). The corresponding charge densities are shown in Figure 5b, and the blue and yellow regions indicate electron depletion and accumulation, respectively. The larger electron cloud and the greater charge transfer suggest the higher single-molecule adsorption energy in the case of DA. Therefore, more DA molecules are adsorbed and contribute to the current, allowing one to easily differentiate between AA and DA. While at potentials of 0.6 and 0.9 V, the adsorption energies of AA and DA are comparable, and the number of molecules adsorbed is virtually identical. Thus, the response current is similar, making it difficult to distinguish AA from DA at 0.6 and 0.9 V.

For the continuous sensing of DA, a double-molecule adsorption model is applied. The basic principle of double-molecule adsorption is that the adsorption energies of two molecules are close enough to allow adsorption of the other molecule. Figure 5c shows that when the potential is 0.6 V, the adsorption energy of DA is −1.739 eV, which is similar to the single-molecule adsorption energy of DA (−1.984 eV). This favors the adsorption of another molecule, resulting in the highest sensitivity of the sample, as visually reflected in Figure 5d, where the size of the cloud is larger at 0.6 V. The phenomenon that the adsorption energy of the second DA molecule is relatively lower than single-molecule adsorption can be explained by a coeffect of the high electronegativity of the benzene ring of the DA molecule and the increased repulsion effect in a strong electric field.[54] Calculations based on DFT confirm the large difference in single-molecule adsorption energies of DA and AA at appropriate potentials, which leads to the observed good selectivity, while the double-molecule adsorption energy decides the sensitivity.

CONCLUSIONS

In summary, the Fe-HPSW-C composite is fabricated by assembling a MIL-53 (Fe) film on marine biological carbon and an ALD ZnO nanomembrane as an induction layer is adopted for coating with good conformality and firm adhesion. By controlling the concentration of the solution and the parameters of ALD, the geometry and structure of the composite can be tuned to achieve enhanced electrochemical performance. The composite with a hierarchically porous structure and large surface area demonstrates effective active site exposure and the ability of selective adsorption of DA. The composite demonstrates excellent DA sensing performance in terms of a high sensitivity of 2084.58 μA mM^{-1} cm^{-2}, a low LOD of 0.73 μM, and good distinction of DA and AA at a potential of 0.3 V. DFT calculations confirm the large difference in single-molecule adsorption energies of DA and AA at appropriate potentials, which leads to the observed good selectivity. This study provides a new strategy to fabricate

https://doi.org/10.1021/acsami.2c20517
ACS Appl. Mater. Interfaces 2023, 15, 12005−12016

advanced DA sensors and has great potential in biosensing-related fields. We believe that the combination of natural materials and MOFs can be used as a general platform for sensing different bioinformatics molecules.

EXPERIMENTAL SECTION

Materials. Anhydrous ferric chloride ($FeCl_3$) was purchased from Aladdin Ltd. (Shanghai, China). D(+)-GL monohydrate (AR, ≥99.7%), LA (AR, ≥99.7%), *N*,*N*-dimethylformamide (DMF), trifluoroacetic acid (AR, ≥99.7%), and potassium ferricyanide ($K_3[Fe(CN)_6]$) were obtained from Sinopharm Chemicals. DA hydrochloride (≥97%), ascorbic acid (≥99.99%), and benzene-1,4-dicarboxylic acid ($C_8H_6O_4$) were purchased from Aladdin Ltd. (Shanghai, China). The solution used for the electrochemical activity measurements was 0.1 M PBS. All of the reagents were used as received without further purification. Deionized (DI) water used throughout all experiments was purified by a Millipore system.

Fabrication of Marine Biological Carbon. Natural seaweed was obtained from the commercial market. The dried seaweed was carbonized in a tube furnace for 2 h at 800 °C in a N_2 atmosphere. The obtained marine biological carbon (SW-C) was washed with 1 mM hydrochloric acid for 24 h. The natural carbon powder was produced by drying at 60 °C for 24 h.

Fabrication of the Oxide Nanomembrane as the Induction Layer. The ZnO nanomembrane was deposited as an induction layer by ALD. The deposition of the ZnO nanomembrane on the exposed surface of SW-C was performed at 150 °C in an ALD reactor. Diethylzinc (DEZ) and DI water were used as precursors. A typical ALD cycle included a DEZ pulse (50 ms), waiting time (10 s), a N_2 purge (30 s), a DI water pulse (30 ms), waiting time (10 s), and a N_2 purge (30 s). The thickness of the ZnO nanomembrane was precisely controlled by the number of ALD cycles.

Synthesis of the Middle-Thickness MIL-53 (Fe) Film on the Substrates. Anhydrous ferric chloride ($FeCl_3$, 1.62 g) was dissolved in *N*,*N*-dimethylformamide (DMF) (100 mL) to form solution A. 1,4-Dicarboxybenzene (H_2BDC) (1.66 g) was dissolved in DMF (100 mL) to achieve solution B. The ALD ZnO-coated substrates were then well mixed in a beaker containing solution A. The beaker was sealed at 150 °C for 24 h. After cooling to room temperature (formation of the Fe-hydroxy double salt), solution B was added and the mixture was sealed at 150 °C for an additional 24 h. Afterward, the samples were filtered by a vacuum filter and then vacuum-dried at 60 °C for 12 h. After this process, a uniform MIL-53 (Fe) film formed on the surface of the substrates. For electrochemical testing, the obtained sample was washed in an ultrasonic cleaner for 1 h and dried at 60 °C for 12 h.

Synthesis of the Thick MIL-53 (Fe) Film on the Substrates. Similar to the previous preparation method, the thick MIL-53 (Fe) film was prepared in the same way, except that the concentration of the reactants was controlled. In this work, double concentrations (3.24 g $FeCl_3$ and 3.32 g H_2BDC) were used to obtain the thick film.

Synthesis of the Thin MIL-53 (Fe) Film on the Substrates. Similar to the previous synthesis, the thin MIL-53 (Fe) film was prepared in the same way, except that the concentration of the reactants was controlled. In this work, experiments were performed with reagents at half-concentrations (0.81 g $FeCl_3$ and 0.83 g H_2BDC) to obtain the thin film.

Structural and Compositional Characterizations. The morphologies of all of the products were characterized by field-emission SEM using a VEGA TS 5136 MM (TESCAN Co., Czech) system. The cross-sectional morphology was characterized by TEM (JEM-2100F). XRD patterns were achieved by an X'Pert Pro X-ray diffractometer equipped with Cu Ka radiation (λ = 0.1542 nm) at a current of 40 mA and voltage of 40 kV. A Quadrasorb adsorption instrument (Quantachrome Instruments) was used to perform the nitrogen sorption/desorption measurements. The specific surface area was calculated by the BET method. The pore size distributions were calculated from the nitrogen sorption data by the NLDFT model for slit pores provided by Quantachrome data reduction software ASiQwin Version 4.01. EDS (Oxford X-Max 80T) was utilized to analyze the composition of the sample. XPS analyses were performed with a VG ESCALAB 220I-XL equipment. The curve fitting of all XPS spectra was accomplished by XPS Peak 4.1 software. Raman spectra were recorded on a Horiba LabRAM HR Evolution under the excitation of a 532 nm laser. The X-ray absorption spectra (XAS) including XANES and EXAFS of the samples at Fe K-edge were collected at the Singapore Synchrotron Light Source (SSLS) center, where a pair of channel-cut Si (111) crystals was used in the monochromator. The Fe K-edge XANES data were recorded in transmission mode. Fe foil, FeO, and Fe_2O_3 were used as references. The storage ring was working at an energy of 2.5 GeV with an average electron current of below 200 mA. The acquired EXAFS data were extracted and processed according to the standard procedures by the ATHENA module implemented in the FEFIT software packages. The k^3-weighted FT of $x(k)$ in R space was obtained over the range of 0–14.0 $Å^{-1}$ by applying a Besse window function.

Characterization of Electrochemical Sensing Performance. The electrochemical DA sensing performance was evaluated on a CHI 660E (Chenhua Instrument, Shanghai, China) with a three-electrode configuration. In this work, Ag/AgCl (in saturated KCl solution) was used as the reference electrode, a graphite rod was used as the counter electrode, and samples were used as the working electrodes. The sample like the Fe-HPSW-C composite was ground into powder, and Nafion (5 wt %) was used as an adhesive and protective film to stick the sample to glassy carbon (GC; diameter, 5 mm). Before this, the bare GC was polished to a mirror surface with 0.3 μm alumina slurries and then sonicated in ethanol and deionized water alternately several times. Finally, the prepared electrode was dried under infrared light.

Theoretical Model. First-principles calculations were carried out on the basis of periodic DFT by a generalized gradient approximation within the Perdew–Burke–Ernzerhof exchange–correction function. The wave functions were constructed from the expansion of plane waves with an energy cutoff of 500 eV. The γ-centered k-point of 2 × 2 × 1 was used for geometry optimization. The consistency tolerances for the geometry optimization were set as 1.0×10^{-5} eV/atom for total energy and 0.05 eV/Å for force, respectively. To avoid the interaction between the two surfaces, a large vacuum gap of 15 Å was selected in the periodically repeated slabs. The adsorption energy E_{ads} was calculated according to the standard formula: $E_{ads} = E_{Total} - E_{Cat} - E_{Molecular}$, where E_{Total} is the total energy, E_{Cat} is the catalyst energy, and $E_{Molecular}$ is the molecular energy.

ASSOCIATED CONTENT

Supporting Information

The Supporting Information is available free of charge at https://pubs.acs.org/doi/10.1021/acsami.2c20517.

Additional SEM images, additional TEM images, detailed EXAFS results and their fittings, detailed XPS results, additional CV results, additional I–t curves, additional XRD results, statistics of the current responses, and calculated charge density diagrams (PDF)

AUTHOR INFORMATION

Corresponding Authors

Zhe Zhao − *Department of Materials Science, Fudan University, Shanghai 200433, P. R. China; Shanghai Frontiers Science Research Base of Intelligent Optoelectronics and Perception, Institute of Optoelectronics, Fudan University, Shanghai 200433, P. R. China; International Institute for Intelligent Nanorobots and Nanosystems, State Key Laboratory of ASIC and Systems, Fudan University, Shanghai 200438, P. R. China*; Email: zzhao@fudan.edu.cn

Gaoshan Huang − *Department of Materials Science, Fudan University, Shanghai 200433, P. R. China; International*

https://doi.org/10.1021/acsami.2c20517
ACS Appl. Mater. Interfaces 2023, 15, 12005–12016

Institute for Intelligent Nanorobots and Nanosystems, State Key Laboratory of ASIC and Systems, Fudan University, Shanghai 200438, P. R. China; Yiwu Research Institute of Fudan University, Yiwu 322000 Zhejiang, P. R. China; orcid.org/0000-0002-0525-7177; Email: gshuang@fudan.edu.cn

Authors

Xinyi Ke − *Department of Materials Science, Fudan University, Shanghai 200433, P. R. China; Shanghai Frontiers Science Research Base of Intelligent Optoelectronics and Perception, Institute of Optoelectronics, Fudan University, Shanghai 200433, P. R. China; International Institute for Intelligent Nanorobots and Nanosystems, State Key Laboratory of ASIC and Systems, Fudan University, Shanghai 200438, P. R. China*

Jiayuan Huang − *Department of Materials Science, Fudan University, Shanghai 200433, P. R. China*

Chang Liu − *Department of Materials Science, Fudan University, Shanghai 200433, P. R. China*

Ji Tan − *State Key Laboratory of High Performance Ceramics and Superfine Microstructure, Shanghai Institute of Ceramics, Chinese Academy of Sciences, Shanghai 200050, P. R. China*

Hongqin Zhu − *Department of Materials Science, Fudan University, Shanghai 200433, P. R. China; State Key Laboratory of High Performance Ceramics and Superfine Microstructure, Shanghai Institute of Ceramics, Chinese Academy of Sciences, Shanghai 200050, P. R. China*

Zhijia Xiao − *Department of Materials Science, Fudan University, Shanghai 200433, P. R. China; International Institute for Intelligent Nanorobots and Nanosystems, State Key Laboratory of ASIC and Systems, Fudan University, Shanghai 200438, P. R. China*

Xuanyong Liu − *State Key Laboratory of High Performance Ceramics and Superfine Microstructure, Shanghai Institute of Ceramics, Chinese Academy of Sciences, Shanghai 200050, P. R. China;* orcid.org/0000-0001-9440-8143

Yongfeng Mei − *Department of Materials Science, Fudan University, Shanghai 200433, P. R. China; Shanghai Frontiers Science Research Base of Intelligent Optoelectronics and Perception, Institute of Optoelectronics, Fudan University, Shanghai 200433, P. R. China; International Institute for Intelligent Nanorobots and Nanosystems, State Key Laboratory of ASIC and Systems, Fudan University, Shanghai 200438, P. R. China; Yiwu Research Institute of Fudan University, Yiwu 322000 Zhejiang, P. R. China;* orcid.org/0000-0002-3314-6108

Junhao Chu − *Department of Materials Science, Fudan University, Shanghai 200433, P. R. China; Shanghai Frontiers Science Research Base of Intelligent Optoelectronics and Perception, Institute of Optoelectronics, Fudan University, Shanghai 200433, P. R. China*

Complete contact information is available at: https://pubs.acs.org/10.1021/acsami.2c20517

Notes

The authors declare no competing financial interest.

■ ACKNOWLEDGMENTS

This work is supported by the National Key Technologies R&D Program of China (2021YFA0715302 and 2021YFE0191800), the National Natural Science Foundation of China (61975035 and 52203328), the Science and Technology Commission of Shanghai Municipality (22ZR1405000 and 20501130700), the China Postdoctoral Science Foundation (2022TQ0067), and the Open Fund of the State Key Laboratory on Integrated Optoelectronics (IOSKL2016KF08).

■ REFERENCES

(1) Zhao, Y.; Zeng, H.; Zhu, X.-W.; Lu, W.; Li, D. Metal−Organic Frameworks as Photoluminescent Biosensing Platforms: Mechanisms and Applications. *Chem. Soc. Rev.* **2021**, *50*, 4484−4513.

(2) McConnell, E. M.; Cozma, I.; Mou, Q.; Brennan, J. D.; Lu, Y.; Li, Y. Biosensing with DNAzymes. *Chem. Soc. Rev.* **2021**, *50*, 8954−8994.

(3) Herrmann, A.; Haag, R.; Schedler, U. Hydrogels and Their Role in Biosensing Applications. *Adv. Healthcare Mater.* **2021**, *10*, No. 2100062.

(4) Rizwan, K.; Rahdar, A.; Bilal, M.; Iqbal, H. M. N. MXene-Based Electrochemical and Biosensing Platforms to Detect Toxic Elements and Pesticides Pollutants from Environmental Matrices. *Chemosphere* **2022**, *291*, No. 132820.

(5) Nobili, A.; Latagliata, E. C.; Viscomi, M. T.; Cavallucci, V.; Cutuli, D.; Giacovazzo, G.; Krashia, P.; Rizzo, F. R.; Marino, R.; Federici, M.; De Bartolo, P.; Aversa, D.; Dell'Acqua, M. C.; Cordella, A.; Sancandi, M.; Keller, F.; Petrosini, L.; Puglisi-Allegra, S.; Mercuri, N. B.; Coccurello, R.; Berretta, N.; D'Amelio, M. Dopamine Neuronal Loss Contributes to Memory and Reward Dysfunction in A Model of Alzheimer's Disease. *Nat. Commun.* **2017**, *8*, No. 14727.

(6) Muzzi, C.; Bertocci, E.; Terzuoli, L.; Porcelli, B.; Ciari, I.; Pagani, R.; Guerranti, R. Simultaneous Determination of Serum Concentrations of Levodopa, Dopamine, 3-O-Methyldopa and α-Methyldopa by HPLC. *Biomed. Pharmacother.* **2008**, *62*, 253−258.

(7) Peaston, R. T.; Weinkove, C. Measurement of Catecholamines and Their Metabolites. *Ann. Clin. Biochem.: Int. J. Lab. Med.* **2004**, *41*, 17−38.

(8) Nezhad, M. R. H.; Tashkhourian, J.; Khodaveisi, J.; Khoshi, M. R. Simultaneous Colorimetric Determination of Dopamine and Ascorbic Acid Based on the Surface Plasmon Resonance Band of Colloidal Silver Nanoparticles using Artificial Neural Networks. *Anal. Methods* **2010**, *2*, 1263−1269.

(9) Müller, M.; Keßler, B. Deposition from Dopamine Solutions at Ge Substrates: An In Situ ATR-FTIR Study. *Langmuir* **2011**, *27*, 12499−12505.

(10) Sajid, M.; Nazal, M. K.; Mansha, M.; Alsharaa, A.; Jillani, S. M. S.; Basheer, C. Chemically Modified Electrodes for Electrochemical Detection of Dopamine in the Presence of Uric Acid and Ascorbic Acid: A Review. *TrAC, Trends Anal. Chem.* **2016**, *76*, 15−29.

(11) Shin, J.-W.; Kim, K.-J.; Yoon, J.; Jo, J.; El-Said, W. A.; Choi, J.-W. Silver Nanoparticle Modified Electrode Covered by Graphene Oxide for the Enhanced Electrochemical Detection of Dopamine. *Sensors* **2017**, *17*, No. 2771.

(12) Choo, S.-S.; Kang, E.-S.; Song, I.; Lee, D.; Choi, J.-W.; Kim, T.-H. Electrochemical Detection of Dopamine Using 3D Porous Graphene Oxide/Gold Nanoparticle Composites. *Sensors* **2017**, *17*, No. 861.

(13) Ma, F.; Yang, B.; Zhao, Z.; Zhao, Y.; Pan, R.; Wang, D.; Kong, Y.; Chen, Y.; Huang, G.; Kong, J.; Mei, Y. Sonication-Triggered Rolling of Janus Porous Nanomembranes for Electrochemical Sensing of Dopamine and Ascorbic Acid. *ACS Appl. Nano Mater.* **2020**, *3*, 10032−10039.

(14) Hang, T.; Xiao, S.; Yang, C.; Li, X.; Guo, C.; He, G.; Li, B.; Yang, C.; Chen, H.-j.; Liu, F.; Deng, S.; Zhang, Y.; Xie, X. Hierarchical Graphene/Nanorods-Based H_2O_2 Electrochemical Sensor with Self-Cleaning and Anti-Biofouling Properties. *Sens. Actuators, B* **2019**, *289*, 15−23.

(15) Yuan, H.; Zhao, J.; Wang, Q.; Manoj, D.; Zhao, A.; Chi, K.; Ren, J.; He, W.; Zhang, Y.; Sun, Y.; Xiao, F.; Wang, S. Hierarchical Core−Shell Structure of 2D VS2@VC@N-Doped Carbon Sheets Decorated by Ultrafine Pd Nanoparticles: Assembled in a 3D Rosette-

like Array on Carbon Fiber Microelectrode for Electrochemical Sensing. *ACS Appl. Mater. Interfaces* **2020**, *12*, 15507−15516.
(16) Kim, M.; Wang, C.; Earnshaw, J.; Park, T.; Amirilian, N.; Ashok, A.; Na, J.; Han, M.; Rowan, A. E.; Li, J.; Yi, J.; Yamauchi, Y. Co, Fe and N Co-Doped 1D Assembly of Hollow Carbon Nanoboxes for High-Performance Supercapacitors. *J. Mater. Chem. A* **2022**, *10*, 24056−24063.
(17) Kim, M.; Firestein, K. L.; Fernando, J. F. S.; Xu, X.; Lim, H.; Golberg, D. V.; Na, J.; Kim, J.; Nara, H.; Tang, J.; Yamauchi, Y. Strategic design of Fe and N Co-Doped Hierarchically Porous Carbon as Superior ORR Catalyst: From the Perspective of Nanoarchitectonics. *Chem. Sci.* **2022**, *13*, 10836−10845.
(18) Shen, Y.; Pan, T.; Wang, L.; Ren, Z.; Zhang, W.; Huo, F. Programmable Logic in Metal−Organic Frameworks for Catalysis. *Adv. Mater.* **2021**, *33*, No. 2007442.
(19) Dai, Z.; Guo, J.; Su, T.; Wang, J.; Gao, Z.; Song, Y.-Y. Nature-Inspired Mineralization of A Wood Membrane as a Sensitive Electrochemical Sensing Device for In Situ Recognition of chiral molecules. *Green Chem.* **2021**, *23*, 8685−8693.
(20) Zhou, W.; Li, H.; Xia, B.; Ji, W.; Ji, S.; Zhang, W.; Huang, W.; Huo, F.; Xu, H. Selenium-Functionalized Metal-Organic Frameworks as Enzyme Mimics. *Nano Res.* **2018**, *11*, 5761−5768.
(21) Hosseini, H.; Ahmar, H.; Dehghani, A.; Bagheri, A.; Tadjarodi, A.; Fakhari, A. R. A Novel Electrochemical Sensor Based on Metal-Organic Framework for Electro-catalytic Oxidation of L-cysteine. *Biosens. Bioelectron.* **2013**, *42*, 426−429.
(22) Kim, M.; Xin, R.; Earnshaw, J.; Tang, J.; Hill, J. P.; Ashok, A.; Nanjundan, A. K.; Kim, J.; Young, C.; Sugahara, Y.; Na, J.; Yamauchi, Y. MOF-Derived Nanoporous Carbons with Diverse Tunable Nanoarchitectures. *Nat. Protoc.* **2022**, *17*, 2990−3027.
(23) Shahrokhian, S.; Ezzati, M.; Hosseini, H. Fabrication of A Sensitive and Fast Response Electrochemical Glucose Sensing Platform Based on Co-Based Metal-Organic Frameworks Obtained from Rapid In Situ Conversion of Electrodeposited Cobalt Hydroxide Intermediates. *Talanta* **2020**, *210*, No. 120696.
(24) Shahrokhian, S.; Khaki Sanati, E.; Hosseini, H. Direct Growth of Metal-Organic Frameworks Thin Film Arrays on Glassy Carbon Electrode Based on Rapid Conversion Step Mediated by Copper Clusters and Hydroxide Nanotubes for Fabrication of a High Performance Non-Enzymatic Glucose Sensing Platform. *Biosens. Bioelectron.* **2018**, *112*, 100−107.
(25) Ezzati, M.; Shahrokhian, S.; Hosseini, H. In Situ Two-Step Preparation of 3D NiCo-BTC MOFs on a Glassy Carbon Electrode and a Graphitic Screen Printed Electrode as Nonenzymatic Glucose-Sensing Platforms. *ACS Sustainable Chem. Eng.* **2020**, *8*, 14340−14352.
(26) Wang, P.; Li, X.; Zhang, P.; Zhang, X.; Shen, Y.; Zheng, B.; Wu, J.; Li, S.; Fu, Y.; Zhang, W.; Huo, F. Transitional MOFs: Exposing Metal Sites with Porosity for Enhancing Catalytic Reaction Performance. *ACS Appl. Mater. Interfaces* **2020**, *12*, 23968−23975.
(27) Zhao, Z.; Kong, Y.; Huang, G.; Liu, C.; You, C.; Xiao, Z.; Zhu, H.; Tan, J.; Xu, B.; Cui, J.; Liu, X.; Mei, Y. Area-Selective and Precise Assembly of Metal Organic Framework Particles by Atomic Layer Deposition Induction and Its Application for Ultra-Sensitive Dopamine Sensor. *Nano Today* **2022**, *42*, No. 101347.
(28) Kang, D.; Liu, Q.; Gu, J.; Su, Y.; Zhang, W.; Zhang, D. "Egg-Box"-Assisted Fabrication of Porous Carbon with Small Mesopores for High-Rate Electric Double Layer Capacitors. *ACS Nano* **2015**, *9*, 11225−11233.
(29) Zeng, S.; Tang, Z.; Liu, C.; Zhou, P. Electronics Based on Two-Dimensional Materials: Status and Outlook. *Nano Res.* **2021**, *14*, 1752−1767.
(30) Zhao, Y.; Huang, G.; Wang, D.; Ma, Y.; Fan, Z.; Bao, Z.; Mei, Y. Sandwiched Porous C/ZnO/Porous C Nanosheet Battery Anodes with a Stable Solid-Electrolyte Interphase for Fast and Long Cycling. *J. Mater. Chem. A* **2018**, *6*, 22870−22878.
(31) Tang, L.; Lv, Z.-q.; Xue, Y.-c.; Xu, L.; Qiu, W.-h.; Zheng, C.-m.; Chen, W.-q.; Wu, M.-h. MIL-53(Fe) Incorporated in the Lamellar BiOBr: Promoting the Visible-Light Catalytic Capability on the Degradation of Rhodamine B and Carbamazepine. *Chem. Eng. J* **2019**, *374*, 975−982.
(32) Zhang, B.; Dong, G.; Wang, L.; Zhang, Y.; Ding, Y.; Bi, Y. Efficient Hydrogen Production from MIL-53(Fe) Catalyst-Modified Mo:BiVO4 Photoelectrodes. *Catal. Sci. Technol.* **2017**, *7*, 4971−4976.
(33) de Combarieu, G.; Hamelet, S.; Millange, F.; Morcrette, M.; Tarascon, J.-M.; Férey, G.; Walton, R. I. In Situ Fe XAFS of Reversible Lithium Insertion in a Flexible Metal Organic Framework Material. *Electrochem. Commun.* **2009**, *11*, 1881−1884.
(34) Zhang, X.; Liu, Q.; Shi, X.; Asiri, A. M.; Sun, X. An Fe-MOF Nanosheet Array with Superior Activity towards the Alkaline Oxygen Evolution Reaction. *Inorg. Chem. Front.* **2018**, *5*, 1405−1408.
(35) Li, J.; Liu, L.; Ai, Y.; Liu, Y.; Sun, H.; Liang, Q. Self-Polymerized Dopamine-Decorated Au NPs and Coordinated with Fe-MOF as a Dual Binding Sites and Dual Signal-Amplifying Electrochemical Aptasensor for the Detection of CEA. *ACS Appl. Mater. Interfaces* **2020**, *12*, 5500−5510.
(36) Liu, S.; Zhao, Z.; Jin, L.; Sun, J.; Jiao, C.; Wang, Q. Nitrogen-Doped Carbon Networks with Consecutive Conductive Pathways from a Facile Competitive Carbonization-Etching Strategy for High-Performance Energy Storage. *Small* **2022**, *18*, No. 2104375.
(37) Nguyen, D. T. C.; Le, H. T. N.; Do, T. S.; Pham, V. T.; Tran, D. L.; Ho, V. T. T.; Tran, T. V.; Nguyen, D. C.; Nguyen, T. D.; Bach, L. G.; Ha, H. K. P.; Doan, V. T. Metal-Organic Framework MIL-53(Fe) as an Adsorbent for Ibuprofen Drug Removal from Aqueous Solutions: Response Surface Modeling and Optimization. *J. Chem.* **2019**, *2019*, 1−11.
(38) Xiong, W.; Zeng, G.; Yang, Z.; Zhou, Y.; Zhang, C.; Cheng, M.; Liu, Y.; Hu, L.; Wan, J.; Zhou, C.; Xu, R.; Li, X. Adsorption of Tetracycline Antibiotics from Aqueous Solutions on Nanocomposite Multi-Walled Carbon Nanotube Functionalized MIL-53(Fe) as New Adsorbent. *Sci. Total Environ.* **2018**, *627*, 235−244.
(39) Devautour-Vinot, S.; Maurin, G.; Henn, F.; Serre, C.; Devic, T.; Férey, G. Estimation of the Breathing Energy of Flexible MOFs by Combining TGA and DSC Techniques. *Chem. Commun.* **2009**, *19*, 2733−2735.
(40) Zhao, Z.; Kong, Y.; Liu, C.; Huang, G.; Xiao, Z.; Zhu, H.; Bao, Z.; Mei, Y. Atomic Layer Deposition-Assisted Fabrication of 3D Co-Doped Carbon Framework for Sensitive Enzyme-Free Lactic Acid Sensor. *Chem. Eng. J.* **2021**, *417*, No. 129285.
(41) Anibal, J.; Romero, H. G.; Leonard, N. D.; Gumeci, C.; Halevi, B.; Calabrese Barton, S. Effect of Silica Morphology on the Structure of Hard-Templated, Non-Precious Metal Catalysts for Oxygen Reduction. *Appl. Catal., B* **2016**, *198*, 32−37.
(42) Occelli, M. L.; Olivier, J. P.; Perdigon-Melon, J. A.; Auroux, A. Surface Area, Pore Volume Distribution, and Acidity in Mesoporous Expanded Clay Catalysts from Hybrid Density Functional Theory (DFT) and Adsorption Microcalorimetry Methods. *Langmuir* **2002**, *18*, 9816−9823.
(43) Zhao, Z.; Liu, S.; Zhu, J.; Xu, J.; Li, L.; Huang, Z.; Zhang, C.; Liu, T. Hierarchical Nanostructures of Nitrogen-Doped Porous Carbon Polyhedrons Confined in Carbon Nanosheets for High-Performance Supercapacitors. *ACS Appl. Mater. Interfaces* **2018**, *10*, 19871−19880.
(44) Wang, X.; Ba, X.; Cui, N.; Ma, Z.; Wang, L.; Wang, Z.; Gao, X. Preparation, Characterisation, and Desalination Performance Study of Cellulose Acetate Membranes with MIL-53(Fe) Additive. *J. Membr. Sci.* **2019**, *590*, No. 117057.
(45) Gong, C.; Shen, Y.; Chen, J.; Song, Y.; Chen, S.; Song, Y.; Wang, L. Microperoxidase-11@PCN-333 (Al)/Three-Dimensional Macroporous Carbon Electrode for Sensing Hydrogen Peroxide. *Sens. Actuators, B* **2017**, *239*, 890−897.
(46) Nisar, A.; Khan, M. A.; Hussain, Z. Synthesis and Characterization of PANI/MOF-199/Ag Nanocomposite and its Potential Application as Non-Enzymatic Electrochemical Sensing of Dopamine. *J. Korean Ceram. Soc.* **2022**, *59*, 359−369.
(47) Shu, Y.; Lu, Q.; Yuan, F.; Tao, Q.; Jin, D.; Yao, H.; Xu, Q.; Hu, X. Stretchable Electrochemical Biosensing Platform Based on Ni-MOF Composite/Au Nanoparticle-Coated Carbon Nanotubes for

https://doi.org/10.1021/acsami.2c20517
ACS Appl. Mater. Interfaces 2023, 15, 12005−12016

Real-Time Monitoring of Dopamine Released from Living Cells. *ACS Appl. Mater. Interfaces* **2020**, *12*, 49480−49488.
(48) Huang, T.-Y.; Kung, C.-W.; Liao, Y.-T.; Kao, S.-Y.; Cheng, M.; Chang, T.-H.; Henzie, J.; Alamri, H. R.; Alothman, Z. A.; Yamauchi, Y.; Ho, K.-C.; Wu, K. C.-W. Enhanced Charge Collection in MOF-525-PEDOT Nanotube Composites Enable Highly Sensitive Biosensing. *Adv. Sci.* **2017**, *4*, No. 1700261.
(49) Lu, S.; Hummel, M.; Chen, K.; Zhou, Y.; Kang, S.; Gu, Z. Synthesis of Au@ZIF-8 Nanocomposites for Enhanced Electrochemical Detection of Dopamine. *Electrochem. Commun.* **2020**, *114*, No. 106715.
(50) Kavya, K. V.; Muthu, D.; Pattappan, D.; Vargheese, S.; Gokila, N.; Sivaramkumar, M. S.; Kumar, R. T. R.; Haldorai, Y. Palladium Nanoparticles Decorated Ni-MOF Nanocomposite as an Electrochemical Platform for the Selective Detection of Dopamine. *Mater. Lett.* **2022**, *306*, No. 130926.
(51) Pandikumar, A.; How, G. T. S.; See, T. P.; Omar, F. S.; Jayabal, S.; Kamali, K. Z.; Yusoff, N.; Jamil, A.; Ramaraj, R.; John, S. A.; Lim, H. N.; Huang, N. M. Graphene and its Nanocomposite Material Based Electrochemical Sensor Platform for Dopamine. *RSC Adv.* **2014**, *4*, 63296−63323.
(52) Chen, Z.; Wu, R.; Liu, Y.; Ha, Y.; Guo, Y.; Sun, D.; Liu, M.; Fang, F. Ultrafine Co Nanoparticles Encapsulated in Carbon-Nanotubes-Grafted Graphene Sheets as Advanced Electrocatalysts for the Hydrogen Evolution Reaction. *Adv. Mater.* **2018**, *30*, No. 1802011.
(53) Chen, Z.; Ha, Y.; Jia, H.; Yan, X.; Chen, M.; Liu, M.; Wu, R. Oriented Transformation of Co-LDH into 2D/3D ZIF-67 to Achieve Co−N−C Hybrids for Efficient Overall Water Splitting. *Adv. Energy Mater.* **2019**, *9*, No. 1970066.
(54) Zhang, X.; Wan, K.; Subramanian, P.; Xu, M.; Luo, J.; Fransaer, J. Electrochemical Deposition of Metal-Organic Framework Films and their Applications. *J. Mater. Chem. A* **2020**, *8*, 7569−7587.
(55) Bouchaala, A.; Jaber, N.; Yassine, O.; Shekhah, O.; Chernikova, V.; Eddaoudi, M.; Younis, M. I. Nonlinear-Based MEMS Sensors and Active Switches for Gas Detection. *Sensors* **2016**, *16*, No. 758.

https://doi.org/10.1021/acsami.2c20517
ACS Appl. Mater. Interfaces 2023, 15, 12005−12016